

# Variations in the Cyclotron Resonant Scattering Features during 2011 outburst of 4U 0115+63

N. Iyer<sup>1,2\*</sup>, D. Mukherjee<sup>3†</sup>, G.C Dewangan<sup>4‡</sup>, D. Bhattacharya<sup>4§</sup> and S. Seetha<sup>5¶</sup>

<sup>1</sup>ISRO Satellite Centre, Bangalore, India

<sup>2</sup>Indian Institute of Science, Bangalore, India

<sup>3</sup>Research School of Astronomy and Astrophysics, The Australian National University, Canberra, ACT 2611, Australia

<sup>4</sup>Inter-University Centre for Astronomy and Astrophysics, Pune, India

<sup>5</sup>Space Science Office, ISRO HQ, Bangalore, India

Accepted \*\*. Received \*\*, in original form \*\*

## ABSTRACT

We study the variations in the Cyclotron Resonant Scattering Feature (CRSF) during 2011 outburst of the high mass X-ray binary 4U 0115+63 using observations performed with *Suzaku*, *RXTE*, *Swift* and *INTEGRAL* satellites. The wide-band spectral data with low energy coverage allowed us to characterize the broadband continuum and detect the CRSFs. We find that the broadband continuum is adequately described by a combination of a low temperature ( $kT \sim 0.8$  keV) blackbody and a power-law with high energy cutoff ( $E_{cut} \sim 5.4$  keV) without the need for a broad Gaussian at  $\sim 10$  keV as used in some earlier studies. Though winds from the companion can affect the emission from the neutron star at low energies ( $< 3$  keV), the blackbody component shows a significant presence in our continuum model. We report evidence for the possible presence of two independent sets of CRSFs with fundamentals at  $\sim 11$  keV and  $\sim 15$  keV. These two sets of CRSFs could arise from spatially distinct emitting regions. We also find evidence for variations in the line equivalent widths, with the 11 keV CRSF weakening and the 15 keV line strengthening with decreasing luminosity. Finally, we propose that the reason for the earlier observed anti-correlation of line energy with luminosity could be due to modelling of these two independent line sets ( $\sim 11$  keV and  $\sim 15$  keV) as a single CRSF.

**Key words:** X-rays: binaries – pulsars: individual 4U 0115+634

## 1 INTRODUCTION

4U 0115+63 is a high mass X-ray binary system, first discovered in the UHURU satellite's sky survey (Giacconi et al. 1972; Forman et al. 1978), with more than 15 subsequent outbursts recorded till date (Boldin et al. 2013). The system consists of a pulsating neutron star with spin period  $\sim 3.61$  s (Cominsky et al. 1978) and a B0.2Ve main sequence star (Johns et al. 1978), with an orbital period of  $\sim 24.3$  days (Rappaport et al. 1978). The distance to this binary system has been estimated to be  $\sim 7$  kpc (Negueruela & Okazaki 2001). The source exhibits luminous Type II X-ray outburst during which multiple cyclotron resonance scattering features (CRSF) have been observed in the X-ray spec-

trum, with 5 detected harmonics (Santangelo et al. 1999; Ferrigno et al. 2009). CRSF are caused by scattering of X-ray photons from electrons in the accreting plasma channelled by the NS magnetic field. The energy at which these lines occur is given as  $E_{cyc} = 11.6 B_{12} \times (1+z)^{-1}$  keV (Coburn et al. 2002). Here  $B_{12}$  is the local magnetic field (in units of  $10^{12}$  Gauss) and  $z$  is the gravitational redshift in line energy. Thus cyclotron lines give us a direct probe of the local magnetic field near the scattering regions.

Cyclotron line parameters of many sources are found to vary with the phase of rotation (see Heindl et al. 2004, for a review), and the varying luminosity of the outburst (Becker et al. 2012). However, the variation in energy of the fundamental CRSF of 4U 0115+63 with luminosity has been the source of some debate. Nakajima et al. (2006); Tsygankov et al. (2007); Li et al. (2012) find an anti-correlation between the line energy and luminosity, whereas Müller et al. (2013) find this anti-correlation to be an artifact of the continuum spectral modelling. Boldin et al.

\* E-mail: nirmal@physics.iisc.ernet.in

† E-mail: dipanjan.mukherjee@anu.edu.au

‡ E-mail: gulabd@iucaa.ernet.in

§ Email: dipankar@iucaa.ernet.in

¶ E-mail: seetha@isro.gov.in

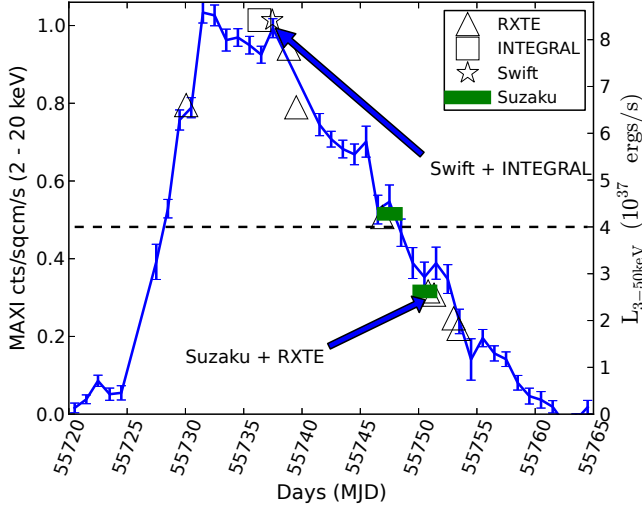


**Figure 1.** Variations in the count rate and luminosity during the 2011 outburst of 4U 0115+63. The continuous line represents the observed count rate measured with the *MAXI* sky monitor. The symbols represent the pointed observations and the corresponding 3 – 50 keV luminosities derived from our spectral analysis. The two simultaneous wide-band observations are annotated separately. The horizontal line shows the luminosity level ( $4 \times 10^{37} \text{ ergs s}^{-1}$ ) around which the previous observations (Li et al. 2012) have found a sharp change in fundamental CRSF energy.

(2013) have pointed out the cause of this reported dichotomy to be due to the use of a broad Gaussian like emission feature to model the continuum in some of the works.

In this paper, we study multiple observations during the 2011 outburst of 4U 0115+63 performed with *Suzaku*, *RXTE*, *Swift* and *INTEGRAL* satellites, providing us with a wide-band coverage from 0.5 keV to  $\sim 60$  keV with high signal-to-noise. As shall be seen in subsequent sections, this availability of wide bandwidth data is very important to correctly model both the continuum and the CRSF in the source spectrum. From the results of our spectral analysis, we find evidence for two sets of cyclotron lines whose parameters vary with source luminosity. In the following sections, we describe the observations and reduction of data that we used in §2, spectral analysis of these data-sets in §3, and the inferences and possible implications in §4

## 2 OBSERVATIONS AND DATA REDUCTION

In all, we analysed data obtained by different X-ray observatories over the 15 days of the 2011 outburst. Table 1 lists all the *RXTE* and *Suzaku* observations which were available in the archive and a *Swift* and an *INTEGRAL* observation, made when the source was near its peak luminosity. Figure 1 shows the variations in the count rates as measured with *MAXI* sky monitor during the 2011 outburst. The pointed observations performed at different luminosity levels are also marked in this figure. The reduction of data-sets from each of these satellites is explained in the following sub-sections.

**Table 1.** A summary of pointed observations during the 2011 outburst of 4U 0115+63.

MJD	Instrument	ObsId	MAXI <sup>a</sup>	Exposure <sup>b</sup>
55730.06	<i>RXTE</i>	96032-01-01-00	0.788	6.53
55736.34	<i>Swift</i>	00031172010	0.925	6.69
55736.34	<i>INTEGRAL</i>	106100650010	0.925	2.13
55738.87	<i>RXTE</i>	96032-01-02-00	0.993	4.52
55739.51	<i>RXTE</i>	96032-01-02-01	0.745	3.69
55743.91	<i>RXTE</i>	96032-01-03-00	0.682	5.02
55746.90	<i>RXTE</i>	96032-01-03-02	0.526	9.04
55747.53	<i>Suzaku</i>	406048010	0.526	24.27
55750.82	<i>RXTE</i>	96032-01-04-00	0.352	16.91
55750.82	<i>Suzaku</i>	406049010	0.352	81.68
55751.32	<i>RXTE</i>	96032-01-04-02	0.388	2.08
55753.00	<i>RXTE</i>	96032-01-04-03	0.248	1.85
55753.42	<i>RXTE</i>	96032-01-04-04	0.238	0.73

<sup>a</sup>MAXI rate (in counts  $\text{cm}^{-2} \text{s}^{-1}$ ) is of nearest observation.

<sup>b</sup>Exposure time is in kilo-seconds.

### 2.1 *RXTE* Observations

Among the *RXTE* observations, we used all but two of them. Obs-Id 96032-01-04-03 and 96032-01-04-04 were made when source flux was very low, and with short exposure times (1856s and 736s respectively). Due to poor count statistics, we were unable to constrain the CRSF parameters for these observations, making them unsuitable for the present work. *RXTE* spectra were obtained from the raw data files using *FTOOLS* from *HEASoft* v 6.15.1. We used data from both the *HEXTE* and the *PCA* detectors. PCU2 Science Array data were used for generating *PCA* spectrum, and Cluster A Science Array data were used for *HEXTE* spectrum. *HEXTE* background was obtained from Cluster B, and dead-time corrections were applied to both the source and background *HEXTE* spectra. For *PCA*, we found the dead-time to be a maximum of 5%, which lowered its flux by about 5%. We did separately correct for this. Data grouping and usage of systematic errors for the *RXTE* spectra are shown in Table 2. In all, the *RXTE* provided usable data covering the 3 keV to 50 keV band.

### 2.2 *Suzaku* Observations

*Suzaku* had two long duration observations made during the course of the 2011 outburst. For reduction of *Suzaku* data, we used *FTOOLS* from *HEASoft* 6.15.1 with *CALDB* updated till June 2014. We used data from the *XIS* (0.6 keV – 10 keV) and *PIN* (15 keV – 60 keV). The *GSO* data had very low SNR and hence was not used. Although the *PIN* does collect data from 12 keV onwards, we discarded the data from 12 keV to 15 keV due to high uncertainty in *PIN* background<sup>1</sup>. *XIS* data above 10 keV and *PIN* data above 60 keV were too noisy to be of use for our analysis. As a result we were not able to effectively cover the energy range (10 keV – 15 keV), which is important to model the fundamental cyclotron line in this system. To overcome this, we used simultaneously taken

<sup>1</sup> see *Suzaku* Data Reduction ABC guide (version 4.0)

*RXTE* observations in conjunction with our *Suzaku* data-sets. Since obs-id 406049010 (*Suzaku*) and Obs-Id 96032-01-04-00 (*RXTE*) had some overlap, we used the portion where overlap existed. This was done by creating a GTI which covered the common interval between the *RXTE* and *Suzaku* GTI files. However Obs-Id 406048010 (*Suzaku*) had no overlap with any other *RXTE* observation. Thus, we did not use this data-set.

The *XIS* data were taken in the 1/4 windowed mode (of size 256 pixels) at normal clocking speeds to reduce the effect of pile-up. We found significant pile-up upto a maximum level of  $\sim 17\%$  in the central regions and corrected for it using the recipe of John Davis<sup>2</sup>. This was achieved by rejecting a central circular region of size  $\sim 25''$  from the *XIS* image for which the computed Pile-up percentage was greater than 6%. After extraction of data from individual *XIS* chips, the *XIS* 0 and 3 data were combined using the *addascaspec* tool. This resulted in two sets of spectral files; one from the back illuminated (BI) CCD and the other from the combined front illuminated (FI) CCDs. *XIS* data below 0.8 keV were rejected owing to discrepancies between the FI and BI spectra at a  $\sim 3\sigma$  level. A mismatch at a  $\sim 2\sigma$  level between the two spectra around the Si K-edge was also noticed, but we did not discard this part of the spectrum as it was important for fitting our continuum model. This led to poorer values of the  $\chi^2$  statistic that we use for fitting the spectral data.

The *PIN* data were extracted using the tool *hxdpinxbpi*. In the joint analysis of *Suzaku* and *RXTE*, we required a cross-normalisation of  $\sim 1.57$ , between the *Suzaku* *XIS* and *PIN*, much larger than the recommended value of 1.16 given in the *Suzaku* Data Reduction ABC guide (version 4.0). Therefore, we investigated this issue in some detail. To verify the *PIN* data, we extracted individual 64 *PIN* count spectrum as explained in the *Suzaku* note on estimating *PIN* noise<sup>3</sup>, and found no discrepancies. We also extracted night-earth data for the *PIN* observations to compare and see if the estimated backgrounds were correct. Fig. 2 compares the night-earth and the “tuned” background spectral data. The two background spectra are similar in shape and in flux.

We further examined the validity of the background subtraction by comparing the net (source minus background) and background light curves. The lack of correlation amongst the two indicates that the *PIN* background was estimated correctly. Finally we checked if the *XIS* spectra were properly area corrected. The *XIS* data were taken in the 1/4 window mode with normal clocking, thereby making a rectangular source footprint. By choosing both rectangular and circular source regions for extraction we found no difference in the resulting spectrum. The difference in the fit-quality as a result of using the recommended and the best-fit cross-normalisation factor, 1.16 and 1.57 respectively, is shown in Figure 3. As seen in the figure, the discrepancy in the ratio plot for *Suzaku* *PIN* (seen as a set offset points in the ratio plot of the left panel) vanishes when we use the best fit cross normalisation factor. We have thus used a cross-

normalisation factor of 1.57 for all our subsequent models and fits (also see Sect. 3).

### 2.3 *Swift* and *INTEGRAL* observation

We selected this particular observation from multiple *Swift* observations of the source, because it was simultaneously taken with an *INTEGRAL* observation (thereby enabling wide-band spectral coverage) and it was near the point having highest *MAXI* counts. This observation gave us a wide-band data-set near the peak luminosity with similar energy coverage to the *Suzaku* data-set at much lower luminosity levels. However, as pointed out in section 3, the low effective area of *INTEGRAL* *JEM-X* resulted in lower signal to noise in the energy band from 11 keV to 17 keV, than for the *Suzaku* data-set.

*Swift* data reduction was carried out using *FTOOLS* from *HEASoft* 6.15.1 with *CALDB* updated till June 2014. *INTEGRAL* analysis was done using *OSA* 10.0 with its calibration files also updated till June 2014. We used the *Swift* *XRT* data from 0.5 keV to 9.7 keV for our spectral analysis. These data were taken in the windowed timing (WT) mode of *XRT*. The maximum observed count rate was about 40 counts s<sup>-1</sup>. This ensured that the *XRT* data was not piled up (see Romano et al. 2006). The *XRT* data from 0.4 keV to 1 keV did show an excess due to uncertainty in the response modelling of *XRT* WT mode, but upon using the position dependent WT response files, this apparent excess was removed<sup>4</sup>. Hence we used these position dependant response files for all our analysis.

We used two instruments - the *JEM-X* and the *IBIS* from the *INTEGRAL*’s suite. The *JEM-X* 2 data (from *JEM-X*) and the *ISGRI* data (from *IBIS*) were extracted with higher spectral binning than used in the standard pipeline. The *JEM-X* data were extracted from 3 keV to 30 keV and the *IBIS* data from 15 keV to 100 keV, as per the instructions in the *IBIS* Analysis User Manual (Issue 10.0). The latest calibration files were used for generating the spectra and the rebinned rmfs. After extraction, the data were grouped and systematic errors added as given in Table 2. We used spin phase averaged spectra in all the observations. For modelling the spectra, we used *XSPEC* v12.8.1g (Arnaud 1996).

## 3 SPECTRAL ANALYSIS

We began our spectral analysis with the wide-band *Suzaku* dataset (obs-id 406049010) taken alongwith *RXTE* dataset (obs-id 96032-01-04-00). For other datasets, we used the results from this analysis as a template because this data-set had both wide-band spectral coverage and high signal to noise. As noted previously, when we held the *PIN-XIS* cross-normalisation fixed at 1.16 we found a significant offset of only the *PIN* spectrum from the other instrument spectrum in the ratio plots (refer Fig. 3 for the best fit *cutoffpl* based model with CRSFs). When we let the normalisation parameter free, we found that it gave a best fit value of 1.57 which we adopted for all our subsequent analysis.

<sup>2</sup> <http://space.mit.edu/CXC/software/suzaku/>

<sup>3</sup> <http://heasarc.gsfc.nasa.gov/docs/suzaku/analysis/pinnoise.html>

<sup>4</sup> <http://www.swift.ac.uk/analysis/xrt/rmfs.php>

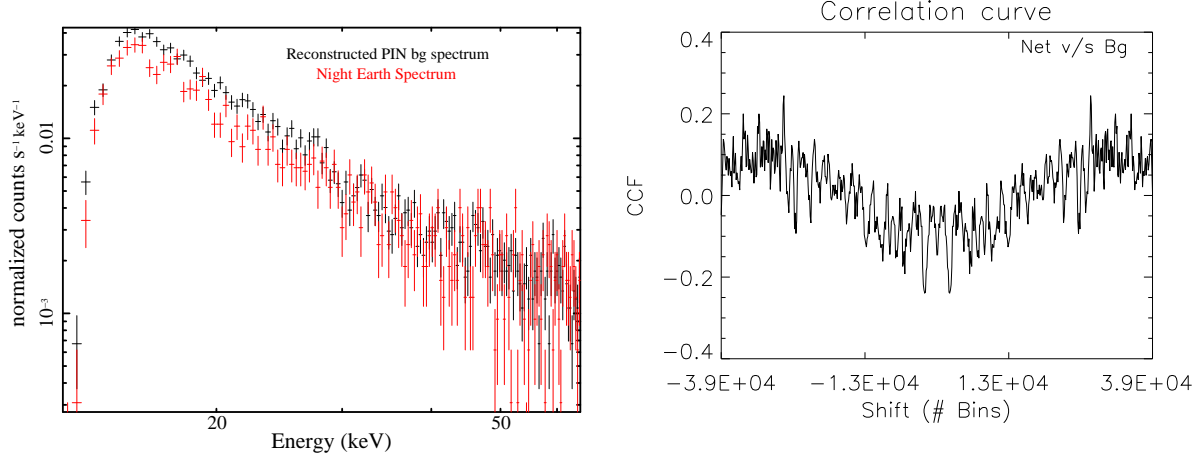


**Figure 2.** A comparison of the estimated tuned *PIN* background and the night-earth *PIN* data. The left panel compares the spectral data extracted from reconstructed *PIN* background and the Night Earth data. See online edition for a color print of this figure. Right panel show the cross-correlation between the net (source - background) and background lightcurves. See text for details.

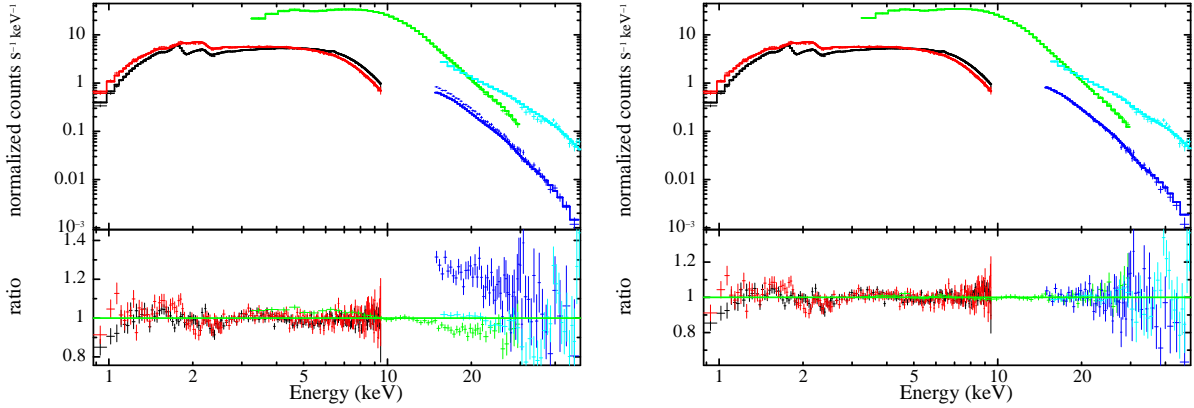


**Figure 3.** The spectral data (*XIS* data in red and black, *PIN* data in dark blue, *PCA* data in green and *HEXTE* in light blue color) and the ratio plots for best-fitting *cutoffpl* model. These plots were made with the *XIS*-to-*PIN* cross-normalisation fixed at 1.16 (left panel) and with the best-fit value of 1.57 (right panel). The offset is seen in the ratio plot in left panel when using a cross-normalisation value of 1.16. See beginning of section 3 for comments on this figure and the online edition for a color print of this figure.

**Table 2.** Grouping scheme and systematic errors used for different spectral datasets.

Spectral data	Grouping scheme	Systematic errors
<i>RXTE</i> PCU	None	1%
<i>RXTE</i> <i>HEXTE</i>	Minimum 60 counts/bin	1%
<i>Suzaku</i> <i>XIS</i>	Minimum 60 counts/bin and oversample by 3	None
<i>Suzaku</i> <i>PIN</i>	Minimum 40 counts/bin	None
<i>Swift</i> <i>XRT</i>	Minimum 60 counts/bin	None
<i>INTEGRAL</i> <i>JEM-X</i> <sup>a</sup>	31 bins in 3–30 keV	3%
<i>INTEGRAL</i> <i>IBIS</i> <sup>a</sup>	27 bins in 15–100 keV	1%

<sup>a</sup> Coded mask datasets have Gaussian and not Poisson statistics and therefore do not need rebinning.

To model this wide-band spectrum, we started off by using the simple *cutoffpl* based continuum modified by interstellar absorption and CRSFs. At low energies ( $< 2$  keV),

effects of local absorption and emission features from the plasma wind of the companion star are known to affect the spectrum (Suchy 2011). However, we did not specifically account for this in the spectrum. Complete modelling of the wind spectrum is preferably done with higher spectral resolution data from gratings. As mentioned in Sec. 2.2, the *Suzaku* data-set had calibration uncertainties around the detector’s Si K-edge (from  $\sim 1.6$  keV to  $\sim 2.5$  keV). Thus modelling the wind effects was difficult with this data-set. As these effects are restricted to lower energies, and as we do not consider data below 0.8 keV in our analysis, we do not expect this to change our continuum model estimates significantly. The interstellar absorption was modelled by an updated version of *tbabs*<sup>5</sup> using abundances of Wilms et al. (2000) and cross-sections as given in Verner & Yakovlev (1995).

This model fit well if we took data above 3 keV, but showed a significant excess when we included the data from

<sup>5</sup> <http://pulsar.sternwarte.uni-erlangen.de/wilms/research/tbabs>

0.8 keV to 3 keV. This is clearly seen in the top left panel of Figure 4, where we obtained  $\chi^2/dof = 2018.60/474$ . On using a blackbody (**bbody**) to account for this excess, we found that the spectral data were well fitted to give a significant improvement in fit  $\chi^2/dof = 731/472$ . The temperature and radius of the blackbody so obtained are listed in Table 3. The radius was computed from the normalisation of the blackbody model **bbody**, which depends on the luminosity and distance to source. The distance was taken as 7 kpc and luminosity was taken as  $L_{bb} = \sigma \cdot T^4 \cdot \text{Area}$ . The blackbody radius is clearly a factor of 10 larger than expected values for a hotspot at the base of the accreting mound. However, given that we might be integrating emission area from the base of the column and that effects of comptonization of this blackbody due to the accreting plasma are not considered, it is likely that these values are over-estimates. We did try the **XSPEC** model given by Farinelli et al. (2012) to see if this was true and found values of blackbody radius to drop to about 6 kms (see Appendix A for details). The large number of free parameters in this model, though, make it difficult to use while testing the CRSF parameters across multiple data-sets.

We also tried using **comptt** model to account for this low energy excess, as indeed was tried in Ferrigno et al. (2009). This gave us an improvement in fit with the  $\chi^2$  reducing from 688/469 to 583/466. This large improvement strongly indicates that the blackbody seed photons are indeed comptonized. The spectral fits for **comptt** were obtained though, for a electron plasma temperature ( $kT_e$ ) of 1.2 keV, a seed photon temperature of 0.2 keV and plasma optical depth ( $\tau$ ) of 35. The **comptt** code itself is meant for use for plasma temperature greater than 2 keV and at such high  $\tau$ , the shape of the spectrum is very similar to the Wien tail of a blackbody. Using the **comptt** model for this Wien tail alone, also lead to an increase in the value of the absorption column from  $N_H = 1.3 \times 10^{22} \text{ cm}^{-2}$  to  $N_H = 1.7 \times 10^{22} \text{ cm}^{-2}$ . When we tried the same model in the *Swift* / *INTEGRAL* spectrum, we found a very small reduction in the fit statistic  $\chi^2$  from 146/166 to 145/163. Furthermore, none of the *RXTE* observations gave an improvement in fit  $\chi^2$  when using the **comptt** model as compared to the **bbody** model. Finally, we found very little differences in the CRSF energies, while using the simple blackbody model as compared to the comptonized blackbody. Since the data that we analysed could not help us pin down the nature of the low energy continuum, we used the simple blackbody for all subsequent analysis. However, we do note that probing this component further may be important to understand the overall continuum, which in turn may affect the cyclotron line results.

As stated in Suchy (2011) and Müller et al. (2013), we found the column density ( $N_H$ ) to be strongly correlated with the power-law index ( $\Gamma$ ) and to be varying across observations. To prevent any unwanted effects due to changing  $N_H$  on our fits, we fixed the column density for all observations to the best fit value of  $N_H = 1.3 \times 10^{22} \text{ cm}^{-2}$  obtained from the wide-band *Suzaku* observation. We also used a narrow emission line with its centroid fixed at 6.4 keV and width fixed at  $10^{-4}$  keV to model the Fe K- $\alpha$  fluorescence emission which has been observed in many other HMXB NS binary systems and is also expected to be seen in 4U 0115+63 (Torréjon et al. 2010; Müller et al. 2013). For the wide-band *Suzaku* observation, this narrow Fe-line component gave an

**Table 3.** Blackbody radius and area for different observations. Note that *RXTE* observations have higher errors.

Instrument	Day (MJD)	kT ( keV ) <sup>a</sup>	Radius (kms) <sup>b</sup>
<i>RXTE</i>	55730.06	$1.05^{+0.18}_{-0.19}$	$13.12^{+3.78}_{-5.66}$
<i>Swift</i> / <i>INTEGRAL</i>	55736.34	$0.93^{+0.41}_{-0.29}$	$17.39^{+4.31}_{-9.22}$
<i>RXTE</i>	55738.87	$0.94^{+0.65}_{-0.29}$	$17.38^{+6.65}_{-15.36}$
<i>RXTE</i>	55739.51	$1.09^{+0.0}_{-0.20}$	$14.69^{+0.0}_{-6.24}$
<i>RXTE</i>	55743.91	$0.79^{+0.21}_{-0.0}$	$19.57^{+6.47}_{-0.0}$
<i>RXTE</i>	55747.90 <sup>c</sup>	$0.78^{+0.0}_{-0.01}$	$18.85^{+0.0}_{-0.42}$
<i>Suzaku</i> / <i>RXTE</i>	55750.82	$0.73^{+0.01}_{-0.26}$	$13.95^{+0.41}_{-3.61}$
<i>RXTE</i>	55751.32	$0.92^{+0.38}_{-0.0}$	$10.54^{+5.37}_{-0.0}$

<sup>a</sup> All errors in this table are  $1\sigma$  deviations

<sup>b</sup> calculated as  $\sqrt{\frac{\text{area}}{\pi}}$

<sup>c</sup> Could not put error constraints on blackbody temperature

**Table 5.** Continuum parameters for the two wide-band observations

Parameter	<i>Swift</i> / <i>INTEGRAL</i>	<i>Suzaku</i> / <i>RXTE</i>
$N_H(10^{22} \text{ cm}^{-2})$	1.3	1.3
$\Gamma$	$-2.16^{+1.10}_{-0.99}$	$-1.25^{+0.07}_{-0.20}$
$E_{cut}$ keV	$4.81^{+1.22}_{-0.19}$	$5.34^{+0.21}_{-0.01}$
$kT_{bb}$ keV	$0.94^{+0.41}_{-0.0}$	$0.73^{+0.01}_{-0.0}$
$bb_{norm} (x 10^{-3})$	$15.5^{+1.7}_{-1.6}$	$3.7^{+0.2}_{-0.2}$
Fe line eq.width ( eV)	$11.7^{+11.7}_{-20.5}$	$11.7^{+3.0}_{-3.4}$

improvement in  $\chi^2/dof$  from 756/473 to 731/472. Upon testing this with the *simftest* script of **XSPEC**, we found it to be significant to a level greater than  $3\sigma$  for 480 iterations. This test was done using XIS data only, to isolate any effects of the continuum beyond 10 keV.

We model the CRSFs using a symmetric Lorentzian like absorption feature **cyclabs** (Mihara et al. 1990), with each line energy being independently determined by the fit. This was done to account for anharmonic line ratios which can occur due to effects of viewing geometry and asymmetric emission patterns, as has been reported in other HMXB sources (Kreykenbohm et al. 2002; Pottschmidt et al. 2005) and in theoretical simulations (Nishimura 2005; Schönherr et al. 2007; Mukherjee & Bhattacharya 2012; Mukherjee et al. 2013).

Modelling the *Suzaku* spectrum, we found cyclotron lines to be at  $\sim 14$  keV,  $\sim 21$  keV and  $\sim 31$  keV. However, we additionally noted an absorption feature at 11 keV in the fit residuals. Modelling this using a Lorentzian like absorption feature gave a significant improvement in the fit as seen in Fig. 4, with the  $\chi^2/dof$  changing from 731/472 to 688/469. We were not able to fit for any CRSF features above 35 keV in any of the datasets because of large noise at the higher energies. And the CRSF at  $\sim 33$  keV was itself constrained by keeping its FWHM fixed at 4 keV (Ferrigno et al. 2009; Müller et al. 2013). The 4 CRSFs obtained in this observation (as listed in Table 4) are at about 11 keV, 15 keV, 20 keV and 33 keV.

We tried next to model the high luminosity wide-band data of *Swift* and *INTEGRAL* simultaneous observation. We

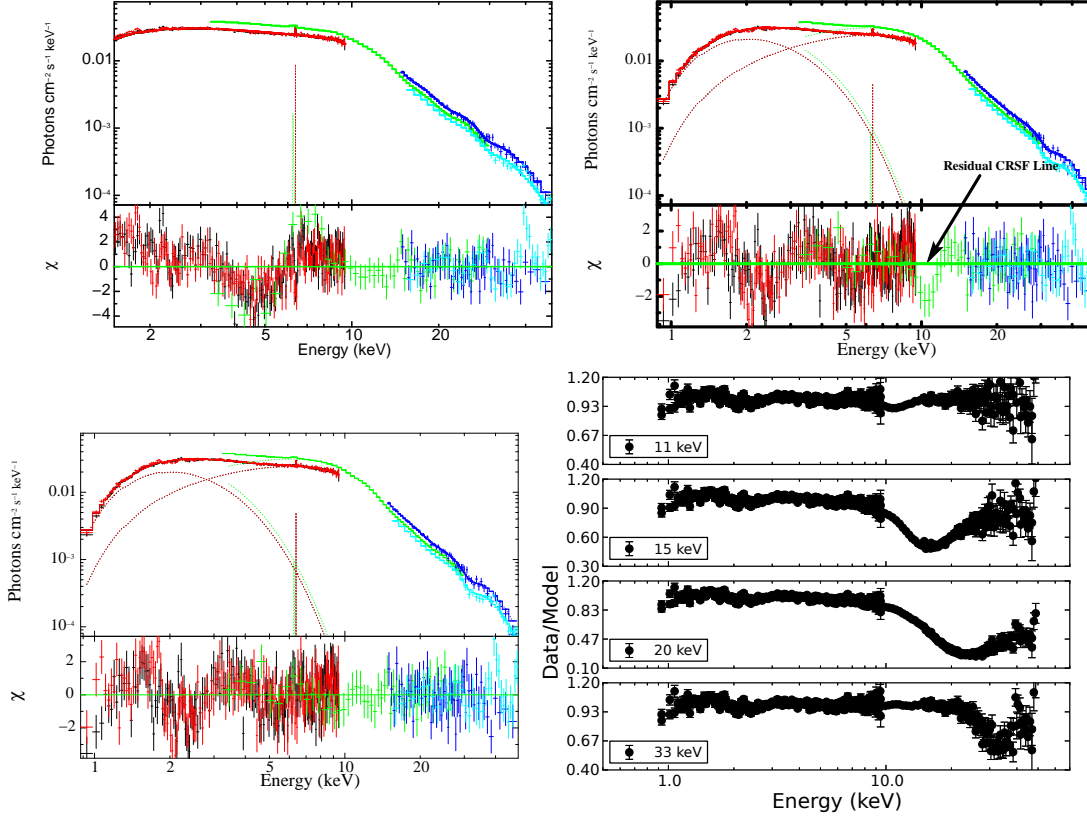


**Figure 4.** Results of our joint spectral fits to the *Suzaku* *XIS* (black and red), *PIN* (blue) and *RXTE* *PCA* (green) and *HEXTE* (light blue) data using a cut-off power-law, CRSFs and a narrow iron K $\alpha$  line at 6.4 keV. Top left: Unfolded spectral data, the model fitted above 3 keV and extended to lower energies in the upper panel and the deviations of the data from the model in the lower panel showing an excess at lower energies. Top right: Similar to top left but the model includes a low temperature blackbody in addition to the cutoffpl and 3 CRSFs. The residuals show possible presence of a 4th cyclotron line at  $\sim 11$  keV. Bottom left: Similar to top right but the model includes a 4th cyclotron line at 11 keV. Bottom right: The 4 cyclotron lines as seen in the ratio plots obtained by setting the optical depth of the lines to zero after obtaining the best fit. See online edition for a color print of this figure.

were able to fit the spectrum from 0.5 keV upto 60 keV using only the *cutoffpl* continuum with absorption fixed at  $N_H = 1.3 \times 10^{22} \text{ cm}^{-2}$  and CRSFs ( $\sim 11$  keV, 20 keV and 33 keV) to get a  $\chi^2/\text{dof} = 172.8/168$ . On adding the blackbody component, this improved to  $\chi^2/\text{dof} = 146.1/166$ . We tested the significance of this using the *lrt* script of *XSPEC*. This gave a significance of greater than  $3\sigma$  for the blackbody model for 408 iteration runs. When taken along with the case of *Suzaku* / *RXTE* data-set, we see that the presence of a soft X-ray component is justified. As stated above, modeling this component is important. For the sake of consistency, we use the blackbody model, as using the *comptt* model for the soft X-ray component did not give us any improvement over the blackbody based model for this observation. While using this blackbody and cutoffpl continuum, we could not fit this data-set with the 5th line as earlier and the fit was consistent with only 3 CRSFs. A summary of the continuum parameters obtained for the two wide-band data-sets is given in Table 5. Errors, unless otherwise mentioned are quoted for a level of 90% confidence in all cases.

We finally analysed the set of standalone *RXTE* observations. Due to the lack of coverage of the low energy bands in these data-sets, it was difficult to constrain the blackbody parameters. Hence we fit the blackbody by starting from a

guess value based on the fit parameters obtained from the wide-band data-set and let the fit routine converge to give the values as quoted in Table 3. The blackbody temperature was frozen to this best fit value while computing errors on other fit parameters. Excepting one, all the *RXTE* data-sets gave an improvement in the fit statistic when using 4 CRSFs as compared to the fit with 3 CRSFs (see Table 4). The exception was the first data-set, taken during the rising phase, which needed only two CRSFs to describe the spectrum. We consider this case separately in the Sec. 4. Given this improvement when using 4 CRSFs, we decided to test its statistical significance for describing the spectral data.

### 3.1 Statistical significance of the 4<sup>th</sup> cyclotron line

Computing detection significance of CRSFs must be handled differently from the standard techniques usually employed for emission features. First, following the method outlined in Orlandini et al. (2012) we construct the F-statistic directly as a ratio of the normalised fit  $\chi^2$  (Orlandini et al. 2012; Bevington & Robinson 1992), as against using the standard F-test implemented in *XSPEC*, which constructs the F-stat as a ratio of change in normalised  $\chi^2$  to the original  $\chi^2$ .

**Table 4.** Best-fit parameters for the CRSFs.

Day (MJD)	Ecyc ( keV )	FWHM ( keV )	$\tau$	$\chi^2/\text{dof}$	Eq. width ( keV )	$\Delta\chi^2 / \Delta\text{dof}^a$	F-stat %
55730.06 ( <i>RXTE</i> )	$16.33^{+0.59}_{-0.32}$ $37.29^{+1.08}_{-1.15}$	$9.38^{+0.56}_{-0.76}$ $4.0^{+0.0}_{-0}$	$1.43^{+0.13}_{-0.16}$ $0.45^{+0.14}_{-0.14}$	57 / 73	$11.98 \pm 0.72$ $2.38^b$	0 / 0	0
55736.34 ( <i>Swift</i> / <i>INTEGRAL</i> )	$10.31^{+1.05}_{-4.58}$ $20.00^{+8.21}_{-6.07}$	$5.96^{+4.58}_{-3.63}$ $9.92^{+5.24}_{-2.19}$	$0.97^{+0.31}_{-0.62}$ $1.26^{+0.31}_{-0.36}$	146 / 166	$6.21 \pm 4.23$ $11.98 \pm 4.50$	0 / 0	0
55738.87 ( <i>RXTE</i> )	$11.71^{+0.37}_{-0.49}$ $15.82^{+0.57}_{-0.68}$	$4.33^{+1.22}_{-1.06}$ $1.1^{+2.97}_{-1.62}$	$0.62^{+0.25}_{-0.06}$ $0.1^{+0.31}_{-0.16}$	47 / 67	$3.35 \pm 1.18$ $0.17 \pm 0.19$	14.91 / 3	83
55739.51 ( <i>RXTE</i> )	$11.66^{+0.39}_{-2.16}$ $16.08^{+2.16}_{-2.16}$	$5.12^{+1.98}_{-2.05}$ $2.09^{+4.53}_{-2.26}$	$0.74^{+0.2}_{-0.1}$ $0.14^{+0.98}_{-0.22}$	43 / 67	$4.49 \pm 4.56$ $0.42 \pm 1.40$	5.81 / 3	64
55743.91 ( <i>RXTE</i> )	$11.25^{+1.03}_{-1.29}$ $15.2^{+0.72}_{-1.29}$	$4.13^{+5.04}_{-2.37}$ $2.82^{+3.08}_{-1.73}$	$0.45^{+0.33}_{-0.32}$ $0.38^{+0.57}_{-0.42}$	31 / 67	$2.50 \pm 2.94$ $1.44 \pm 2.35$	10.17 / 3	84
55747.90 ( <i>RXTE</i> )	$11.20^{+1.04}_{-0.98}$ $14.93^{+0.83}_{-0.98}$	$3.53^{+4.45}_{-2.01}$ $2.76^{+2.41}_{-1.72}$	$0.33^{+0.39}_{-0.28}$ $0.35^{+0.51}_{-0.32}$	52 / 67	$1.63 \pm 1.11$ $1.33 \pm 1.40$	14.99 / 3	81
55750.82 ( <i>RXTE</i> / <i>Suzaku</i> )	$10.77^{+0.32}_{-0.33}$ $14.39^{+0.35}_{-0.33}$	$0.96^{+0.67}_{-0.92}$ $4.19^{+0.97}_{-1.52}$	$0.12^{+0.04}_{-0.25}$ $0.69^{+0.22}_{-0.19}$	688 / 469	$0.17 \pm 0.10$ $3.48 \pm 1.60$	42.68 / 3	74
55751.32 ( <i>RXTE</i> )	$10.76^{+0.0}_{-0.0}$ $14.51^{+0.95}_{-0.84}$	$4.0^{+0.0}_{-2.1}$ $4.67^{+3.08}_{-1.62}$	$0.26^{+0.15}_{-0.09}$ $0.73^{+0.61}_{-0.62}$	57 / 67	$0.17 \pm 0.10$ $0.37 \pm 0.59$	4.32 / 3	55
	$19.55^{+0.0}_{-1.16}$ $31.98^{+1.56}_{-1.56}$	$8.7^{+13.52}_{-0}$ $4.0^{+0.0}_{-0}$	$1.34^{+0.25}_{-0.7}$ $1.05^{+0.42}_{-0.42}$		$10.90 \pm 1.84$ $4.44^b$		

<sup>a</sup> Change / reduction in  $\chi^2$  on addition of extra CRSF / change in number of dof - denotes the confidence that a 4 CRSF model is better than a 3 CRSF model

<sup>b</sup> Cannot quote error on this, as width is frozen

We try to compute the significance of the 4th CRSF at 11 keV, which we used as stated previously to improve the fit. For the *RXTE*/*Suzaku* joint spectral fit, the above method gave us an F-statistic value of 1.06 with a probability value for occurrence due to random noise (PCI) equal to 0.26. We also noted that ignoring data from 1.6 to 2.5 keV (the energy range with calibration mis-match between the two *XIS* detectors) reduces this probability to 0.24 with very little change in spectral parameters. This is not enough to claim detection of a 4th cyclotron line. The F-stat based test performed above, looks at what fraction of the variance of the data-set can be explained by the model. This test looks at the percentage of data variance that a new model (with all its components) can explain as compared to the percentage of data variance explained by the old model (with all its components). Unaccounted residuals exist in the soft part of our fit spectrum below 3 keV. This might account for the low reduction in percentage variance accounted for by the addition of a cyclotron line at the higher energies (11 keV). We checked each of the other *RXTE* observations individually with this F-test (results listed in Table 4). The broad-

band continuum is not completely sampled by the *RXTE* data alone and this could explain the low improvement in  $\chi^2$  for the individual *RXTE* data-sets. To improve the statistics, we did a joint fitting of all the data-sets using both the 3 CRSF and the 4 CRSF models. In doing this fit, we let the line energies for each observation be independently estimated by leaving them untied. This gave an F-statistic value of 1.07 and a probability of chance occurrence of 0.15 (or a confidence level of 85 %).

Finally, we tried a more robust numerical evaluation of significance from Monte-Carlo simulations. We did this by finding the probability of false detection of the 4th CRSF, assuming the 3 CRSF model to be true. By simulating spectra using the *XSPEC lrt* script, we generated a large number (7438) of simulated data-sets following the continuum model with 3 CRSFs modified by statistical noise. The *lrt* script generates these data-sets by using the fit covariance matrix to make a random draw of the fit parameters. The model so obtained, is convolved with the response matrices of the individual detectors, and statistical (Poisson) noise is added to each such simulated data-set. We searched for the pres-



ence of the 4th cyclotron line in each of these data-sets by trying to fit them with the continuum and 4 cyclotron lines, and compared it to a fit with the continuum and 3 cyclotron lines. We tabulated the  $\chi^2$  fit value for each such effort. To check if the observed 4th CRSF was significant, we compare the statistic of each of the simulation runs against the statistic of the observed data. The form of the statistic we used was the F-stat (*fst*) constructed as mentioned before (see also Sartore et al. 2015). We obtained three instances where the simulated *fst* was as high as the observed *fst*. However, in none of these instances, the 4th CRSF fit with centroid near 11 keV. This gave a PCI of 3 in 7438, or a significance of  $3.5\sigma$  for the observed CRSF at 11 keV.

This result, though needs to be treated with care because of the poor  $\chi^2$  of the original fit (731/472) v/s (688/469). We proceed assuming the 4 CRSF model to be the better one, but only after noting that the poor initial fit could influence the Monte-Carlo results.

We then looked at the validity of the 4 CRSF model in describing other data-sets. All the individual *RXTE* spectra do not have wide-band coverage and have lower spectral resolution than say the combined *Suzaku* / *RXTE* data-set. This could be a reason for the marginal improvement in the  $\chi^2$  statistic. The fact that multiple observations showed signs of 4 CRSF features, with an improvement in  $\chi^2$  would lead to an increased relevance of this detection. Additionally, given that each of these observations gave nearly similar centroid energies for all 4 CRSFs (see Fig. 5) would also increase the significance of our detection.

The possible reasons for two observations not requiring 4 CRSFs to describe their spectra are discussed herewith. The *Swift* and *INTEGRAL* simultaneous observations not fitting with the 4 CRSF model could be either because the line at 15 keV does not exist in this observation, or because the line is too weak to be detected by the *JEM-X* detector due to its much lower collection area and poorer signal to noise than the *RXTE/PCA*. This is where we find the high signal to noise of the combined *Suzaku* / *RXTE* data to be critically important. The *RXTE* standalone observation which did not show 4 CRSFs, though had a high signal to noise all through the expected CRSF energy ranges. We take the detection of only 2 CRSFs in this observation to be a valid result and discuss the possible reasons for non detection in this data-set in the next section.

A useful indicator for evaluating the strength of the absorption lines, and to see if they are physically relevant is the line equivalent width. We computed the equivalent width as

$$EW \text{ (keV)} = \int_{E_1}^{E_2} (1 - e^{(-\tau P(E))}) dE \quad (1)$$

$$P(E) = \frac{(W \frac{E}{E_{cyc}})^2}{(E - E_{cyc})^2 + W^2} \quad (2)$$

where  $P(E)$  is the line profile that we use,  $W$  is FWHM of the line,  $E_{cyc}$  is its energy and  $\tau$  is its depth. By simple error propagation of the variances obtained from the fit covariance matrix, we can get an idea of errors on the estimate. We calculated this for all 4 CRSFs to check for their relevance. The results of such calculations are plotted in Fig. 5. We try to make sense of these results in the next section.

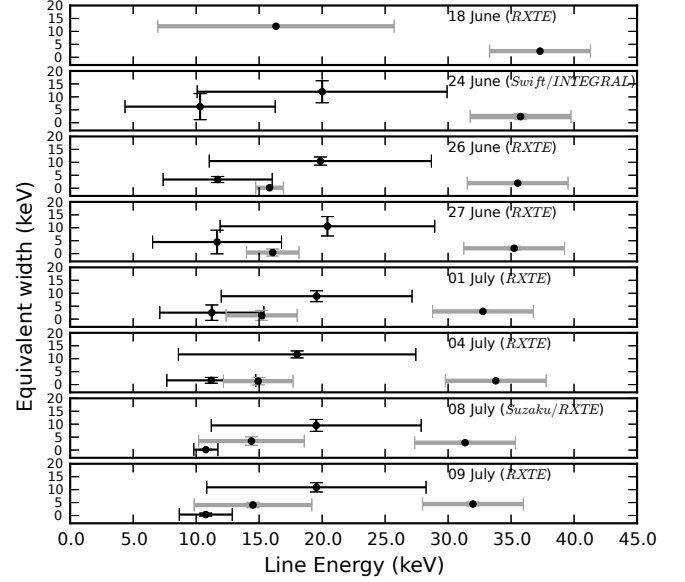


**Figure 5.** Line Distribution diagram. This figure shows the variation in energy, FWHM and equivalent widths of all the lines we obtained in each of our observations. The central point represents the line energy and equivalent width with horizontal bars depicting the FWHM and vertical bars representing errors on the equivalent width. We use black to indicate the 11 keV line set and gray to indicate the 15 keV line set.

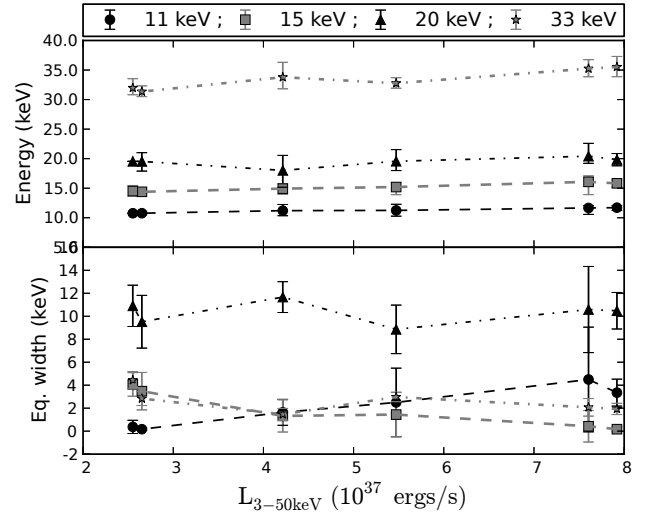


**Figure 6.** 4 CRSFs and their trends with changing luminosity. Top panel shows variation in CRSF energy with luminosity for each of the lines in 4 CRSF model. Bottom panel shows variation in equivalent width for the same set of lines. These plots are made for all data-sets which can be described using 4 CRSFs.

## 4 DISCUSSION

### 4.1 Summary of results

In this work we have analysed the spectra from different X-ray observatories covering the 2011 outburst of the HMXB 4U 0115+63. These include eight observations spread across twenty days including two wide-band observations compris-



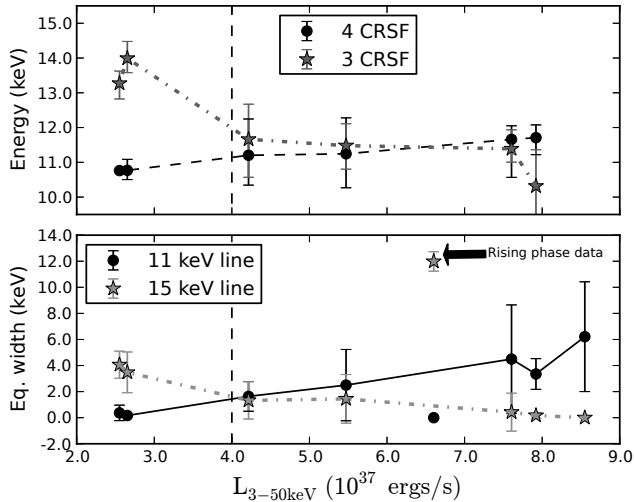


**Figure 7.** Trends in the fundamental lines. Top panel shows the effect of not using 4 CRSF lines, which leads to the anti-correlation with luminosity as reported in previous works. Bottom panel shows the change in line equivalent width of the fundamental of each set of the 4 CRSF model. The vertical line is placed at the same luminosity level as in Fig 1. The rising phase data-set, which does not seem to follow the trend is marked separately. See text for details.

ing of data from multiple satellites (*Swift* + *INTEGRAL* and *Suzaku* + *RXTE*). The use of multiple instruments covering different energy ranges enabled us to properly model the broadband continuum, which in turn yielded better constraints on the CRSFs. The two major results from our analysis are:

(i) **Broadband modelling of the continuum:** The continuum was well constrained with a blackbody component modelling the soft X-ray bands and a cut-off power-law for the harder bands. The blackbody component was found to be statistically significant in both of the wide-band observations, as well as the standalone *RXTE* observations. Excess emission features in the shape of a Gaussian, as reported in previous works e.g. Müller et al. (2013) was not required for our analysis. Such Gaussian features have previously been attributed to possible cyclotron emission (Becker & Wolff 2007; Ferrigno et al. 2014), however such results were inconclusive.

(ii) **Two sets of cyclotron lines:** From the spectral analysis we find evidence for presence of two independent sets of cyclotron lines, each with a harmonic, with fundamental energies centred at  $\sim 11$  keV line and  $\sim 15$  keV line. Previous works find either one of the two fundamental lines, with the 15 keV line found at lower luminosities, and the 11 keV line found at higher luminosities (Tsygankov et al. 2007), resulting in the inference of anti-correlation of the line energy and luminosity. To check whether the 4 cyclotron lines are two independent sets of harmonics we compared the variation of equivalent widths of the lines evaluated following eq. 2. We also investigated variations in line energies with the outburst luminosity (summarised in Figures 5, 6 and 7). We took the line equivalent width of the non-detected line to be zero. From the figures we note that:

(a) There is no luminosity dependence of the fundamental cyclotron line at 11 keV if we use the 4 CRSF model, where both the  $\sim 11$  and  $\sim 15$  keV lines are present. The anti-correlation appears if the 3 CRSF model is used, as shown in the top panel of Fig. 7. This could be an artifact resulting from incorrect spectral modelling with only 3 cyclotron lines, instead of 4 CRSFs, as we discuss below.

(b) In the 4 CRSF model, the line equivalent widths of the two lines at 15 keV and 11 keV show opposite variations with luminosity as seen in the bottom panel of Figure 7.

When only 3 cyclotron lines are used to model the spectra, the two lines at  $\sim 11$  keV and  $\sim 15$  keV are modelled by a single CRSF component. Since the equivalent widths of these two lines changes with luminosity, the single averaged CRSF component is closer to the line with higher equivalent width in the given observation. Simulations have shown that often the second harmonic is deeper and more prominent (Araya-Góchez & Harding 2000; Schönherr et al. 2007) due to photon filling and emission by de-excitation near the fundamental CRSF energy. Results from previous outbursts (Li et al. 2012; Boldin et al. 2013) and our analysis demonstrate the near constant line energy of the 20 keV line. This result too would lead us to expect a near constant line energy for the fundamental 11 keV line.

If we split the 4 CRSFs that we obtained into two sets of harmonics with one at (11 keV and 20 keV) and the other at (15 keV and 33 keV), it helps us explain our observations as listed below :

(a) As shown, this explains the reason for observations of an anti-correlated fundamental CRSF with luminosity.

(b) It could be the reason why this source is the only one to have shown multiple (upto 5) harmonics of the fundamental cyclotron line in its spectrum. If we have two such line forming regions with fundamentals at 11 keV and 15 keV, and each region showed the presence of 2 harmonics, then they can easily be confused for multiple harmonics from a single 11 keV fundamental CRSF.

(c) This would explain why the CRSFs we obtain at 20 keV varies so little, whereas the one we get at 33 keV varies a lot more. Under our hypothesis, the  $\sim 33$  keV line in our observations would be a combination of the 2nd harmonic from the 15 keV set (at  $\sim 30$  keV) and the 3rd harmonic from the 11 keV set (at  $\sim 33$  keV). As seen from Fig. 5 and 6, the  $\sim 33$  keV line shifts to higher energies when the  $\sim 11$  keV line becomes stronger.

(d) Finally, it gives a plausible reason for detection of only two CRSFs in the *RXTE* observation taken during the rising phase. If, for some reason, the 11 keV line set is either not present or has very weak signatures in the rising phase of the outburst, then the observed CRSF energies in the rising phase would correspond to the 15 keV line set only. The values we get for the observed CRSFs seem very close to this.

## 4.2 Possible origin of the cyclotron line sets

In this section we discuss where the two scattering regions could be located and what causes the CRSF strengths from these regions to vary in such a manner.

The first possibility is emission from two different regions at different heights on the same pole. If we assume a dipole like magnetic field structure of the Neutron Star (NS) the difference of  $\sim 4$  keV between two sets of lines can be caused if the difference in height of the emitting regions is  $\sim 1.1$  km, which is approximately the shock height above the neutron star surface (Becker et al. 2012). If the 15 keV line set originates in the fan beam at the base of the mound, and the 11 keV line set in the pencil beam from the top of the shock, then variation in line equivalent widths with luminosity can be explained in terms of varying strengths of the fan and pencil beam emissions. At higher luminosities, the fan beam is expected to dominate, whereas both beams will be visible at intermediate luminosities levels (see Fig. 1 of Becker et al. 2012). However, the effect of such variations of luminosity on the equivalent width is unclear and not adequately addressed by existing theoretical models.

The second possibility is emission from different poles. Sasaki et al. (2012) have analysed the pulse profiles of this source and found a  $\sim 60^\circ$  offset between the position of one of the poles and the antipodal position of the other pole. This non dipolar field structure could lead to different local fields at the scattering regions of each pole, which in turn could cause the difference in energies of the lines formed in each of them. The variation in accretion rate onto one pole as compared to the other can cause the variation in the equivalent widths as seen in bottom panel of Fig. 7.

We can get further indicators by looking at the pulse resolved energy spectrum and pulse phase-lag spectrum. We examined the energy dependant phase lag of the pulses as computed by Ferrigno et al. (2011) for the observation with simultaneous *RXTE/Suzaku* data. We have computed the phase lags using the data from the higher time resolution *RXTE PCA* detector, in a manner similar to that of Ferrigno et al. (2011). As seen in Figure 8, the pulse has two distinct peaks. We obtain the phase lags by taking phases corresponding to the main peak at a reference energy and cross-correlating them against the same set of phase bins at other energies. We have performed this for both the main and secondary peaks, with phase bins taken as shown in bottom panel of Fig. 8. In Ferrigno et al. (2011), the authors report that the most negative phase shifts occur at energies near the CRSF energies. This has been attributed to a change in beam pattern at the CRSF energies, with the photons at the CRSF band lying along a pencil beam whereas the rest of the emission is dominated by a fan beam.

In our analysis, we found that main peak's phase-lag spectrum had a similar set of minima at  $\sim 11$  keV,  $\sim 23$  keV and  $\sim 39$  keV. However, the secondary peak's phase-lag spectrum had minima at  $\sim 16$  keV and  $\sim 30$  keV. The low count rate and increasing errors for energies above 45 keV made it difficult for us to find these dips at higher energies. The phase bins for performing the cross-correlation were chosen in such a manner that the pulse profile at the reference energy band (taken as the band between 8.17 keV to 10.63 keV, similar to Ferrigno et al. (2011)) would have a prominent peak like structure in these phase bins. If we refer to the decomposed pulse profiles in Fig. 8 of Sasaki et al. (2012) for the decay phase of the outburst, we see that the two peaks in our overall pulse profile roughly correspond to the emission from the two poles. This lends support to the two pole possibility. However, we cannot rule out the fan

beam / pencil beam as we have not examined the possible pulse profile and phase lags caused by such a possibility. Modelling these “wavy” phase lags, as attempted before (Ferrigno et al. 2011; Schönherr et al. 2014) could help resolve between these two possibilities. Pulse phase resolved spectra could have given additional indicators. However, the large time resolution of the *Suzaku XIS* data (of 2s) prevented us from getting the spectra at small phase bins of the pulsar spinning at 3.6s.

One way to confirm our hypothesis would be to use a single wide-band large area detector to make similar observations during the next outburst of this source. The constraint of using multiple instruments to bridge over the energy region having CRSFs and the region having the blackbody spectrum makes it very important to have these instruments cross-calibrated properly. While the cross-normalisation constants that we use compare favourably with the calibration carried out by Tsujimoto et al. (2011) for all instruments except *Suzaku PIN-XIS*, we do note that uncertainties in instrument cross-normalisations lead to uncertainties in the computed flux values and line equivalent widths estimated. Having fewer number of instruments to cover the range would then be ideal. For example, five to six snapshot observations over different luminosities using the *XMM Newton* and *NuSTAR* telescopes would definitely give a higher signal to noise data and lesser uncertainty in order to confirm or reject our hypothesis. Another way to do this would be the possible construction of a polarization spectrum. It is a well known fact that cyclotron resonant scattering has highly enhanced cross-sections for incident light polarized in the direction parallel to the local magnetic field, versus its cross-section for light polarized perpendicular to it. This enhancement occurs at the resonant scattering energy and drops off at other energies (see Becker & Wolff 2007, and references there-in). So, potentially a measurement of polarization in small energy bands can pin-point the energy range over which resonant scattering occurs, and effectively delineate the presence of actual CRSFs from those resulting due to incorrect spectral modelling. Future observations by detectors proposed for measuring the polarization in different energy bands (Paul et al. 2010; Hayashida et al. 2014) will definitely help improve our understanding of this problem.

### 4.3 Conclusion

In this paper, we demonstrate the utility of having wide-band high signal to noise data by making use of *Suzaku* and *RXTE* satellite data. Using this, we point out the presence of a blackbody component. We also note the possible indications of two sets of CRSFs in this source. We note that having two sets of lines at 11 keV and 15 keV explains the reason for the observed anti-correlation in the fundamental CRSF energy with source luminosity. It additionally explains the reason for this source being the only known accretion powered pulsar to show 5 harmonics of the fundamental cyclotron line. Data from large area wide-band telescopes like *NuSTAR* and *XMM* or from telescopes which can give a polarization spectrum can potentially help solve this long open problem.

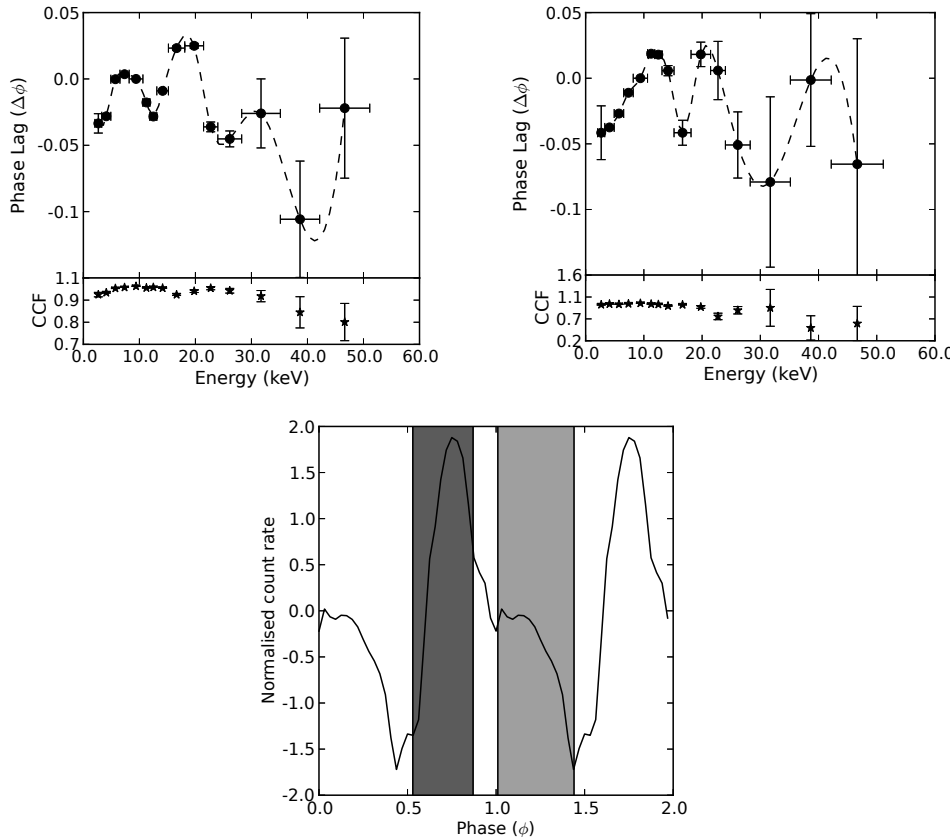


**Figure 8.** Phase lag spectrum and the pulse profile. Bottom panel shows the pulse profile with shaded regions depicting the phase-bins over which correlation was computed. Top left panel is the phase-lag spectrum (and the correlation coefficient) for the Main peak (shaded dark gray in the pulse profile). Top right panel is the phase-lag spectrum from the secondary peak (shaded light gray in the pulse profile).

## ACKNOWLEDGEMENTS

This research has made use of data and software provided by the High Energy Astrophysics Science Archive Research Center (HEASARC), which is a service of the Astrophysics Science Division at NASA/GSFC and the High Energy Astrophysics Division of the Smithsonian Astrophysical Observatory. In addition, it made use of software from INTEGRAL Science Data Centre (ISDC). The data themselves were from obtained from *Suzaku* (TOO proposer K. Pottschmidt), *RXTE* (TOO proposer K. Pottschmidt), *Swift* (TOO proposer S. Müller) and *INTEGRAL* (TOO proposer S. Tsygankov) observatories. We acknowledge these facilities and the proposers for making the observations and providing the data in the archives. We thank Prof. Carlo Ferrigno for some useful pointers regarding the continuum at low energies. We acknowledge the referee's suggestions and comments in helping us firm up the statistical analysis for line significance tests. NI would like to thank Dr. Anil Agarwal, GD, SAG, Mrs. Valaramathi N, DD, CDA and Dr. M. Anandurai, Director, ISAC for continuous support to carry out this research.

## APPENDIX A: FITTING THE CONTINUUM BLACKBODY

The blackbody component that we use for the continuum modelling does not consider effects of compton scattering of this component from the accreting plasma. Farinelli et al. (2012) introduced an *XSPEC* model for implementing this. The results of using this comptonized blackbody are detailed in this section.

There are nine parameters required to describe the comptonized blackbody against two required for the simple blackbody. For getting the model to fit, we had to freeze the plasma parameters to the values obtained by previous attempts to model this source using such a bulk comptonization of seed photons.<sup>6</sup> This model fits for the plasma electron temperature ( $kT_e = 1.3$  keV) and optical depth ( $\tau = 0.41$ ), velocity profile of the accreting plasma (two parameters,  $\eta = 0.5$ ,  $\beta = 0.22$ ), radius of accretion column ( $r_0 = 0.1$ ) and albedo percentage ( $A = 1$ ) from the NS surface (see Table 1 of Farinelli et al. 2012). The remaining free parameters are the blackbody temperature and the model normalization. The results of such a fit are summarized in Table A1. As seen on comparing these results with Table 3, we get blackbody seed temperatures to be similar to the model with a simple blackbody. However, the radius of the

<sup>6</sup> <http://adsabs.harvard.edu/abs/2013A%26A..553A.103F>

**Table A1.** Blackbody temperature and radius for wide-band observations.

Instrument	Day (MJD)	kT ( keV )	Radius (kms) <sup>a</sup>
<i>Swift</i> / <i>INTEGRAL</i>	55736.34	$1.19^{+0.12}_{-0.01}$	$6.67^{+3.28}_{-1.15}$
<i>Suzaku</i> / <i>RXTE</i>	55750.82	$0.76^{+0.01}_{-0.01}$	$6.21^{+1.59}_{-1.15}$

<sup>a</sup> calculated from the normalization parameter

blackbody drops to more reasonable values, although with larger errors. This gives a strong indication that a blackbody component is indeed required to model the spectrum.

## REFERENCES

- Araya-Góchez R. A., Harding A. K., 2000, *ApJ*, 544, 1067
- Arnaud K. A., 1996, in Jacoby G., J. B., eds, *Astronomical Data Analysis Software and Systems V* Vol. 101 of *Astronomical Data Analysis Software and Systems V*, XSPEC: The First Ten Years. p. 17
- Becker P. A., Klochkov D., Schönherr G., Nishimura O., Ferrigno C., Caballero I., Kretschmar P., Wolff M. T., Wilms J., Staubert R., 2012, *A&A*, 544, A123
- Becker P. A., Wolff M. T., 2007, *ApJ*, 654, 435
- Bevington P., Robinson D. K., 1992, *Data Reduction and error analysis for Physical sciences*. 3rd ed., McGraw Hill Higher Education
- Boldin P. A., Tsygankov S. S., Lutovinov A. A., 2013, *Astronomy Letters*, 39, 375
- Coburn W., Heindl W., Rothschild R., Gruber D., Kreykenbohm I., Wilms J., Kretschmar P., Staubert R., 2002, *ApJ*, 580, 394
- Cominsky L., Clark G. W., Li F., Mayer W., Rappaport S., 1978, *Nature*, 273, 367
- Farinelli R., Ceccobello C., Romano P., Titarchuk L., 2012, *A&A*, 538, A67
- Ferrigno C., Becker P. A., Segreto A., Mineo T., Santangelo A., 2009, *A&A*, 498, 825
- Ferrigno C., Falanga M., Bozzo E., Becker P. A., Klochkov D., A. S., 2011, *A&A*, 532, A76
- Ferrigno C., Farinelli R., Bozzo E., 2014, in *The X-ray Universe 2014 The magnetic spectrum of X-ray pulsars*. p. 72
- Forman W., Jones C., Cominsky L., et al. 1978, *ApJ Supplement Series*, 38, 358
- Giacconi R., Murray S., Gursky H., 1972, *ApJ*, 178, 281
- Hayashida K., Yonetoku D., Gunji S., Tamagawa T., Mihara T., et al. 2014, in *Society of Photo-Optical Instrumentation Engineers (SPIE) Conference Series* Vol. 9144 of *Society of Photo-Optical Instrumentation Engineers (SPIE) Conference Series*, X-ray gamma-ray polarimetry small satellite PolariS. p. 0
- Heindl W. A., Rothschild R. E., Coburn W., Staubert R., Wilms J., Kreykenbohm I., Kretschmar P., 2004, in Kaaret P., Lamb F. K., Swank J. H., eds, *X-ray Timing 2003: Rossi and Beyond* Vol. 714 of *American Institute of Physics Conference Series*, Timing and Spectroscopy of Accreting X-ray Pulsars: the State of Cyclotron Line Studies. pp 323–330
- Johns M., Koski A., Canizares C., McClintock J., Rappaport S., Clark G., Cominsky L., Li F., 1978, *IAU Circ.*, 3171, 1
- Kreykenbohm I., Coburn W., Wilms J., Kretschmar P., Staubert R., Heindl W., Rothschild R., 2002, *Å*, 395, 129
- Li J., Wang W., Zhao Y., 2012, *MNRAS*, 423, 2854
- Mihara T., Makishima K., Ohashi T., Sakao T., Tashiro M., 1990, *Nature*, 346, 250
- Mukherjee D., Bhattacharya D., 2012, *MNRAS*, 420, 720
- Mukherjee D., Bhattacharya D., Mignone A., 2013, *MNRAS*, 430, 1976
- Müller S., Ferrigno C., Kühnel M., Schönherr G., Becker P. A., Wolff M. T., Hertel D., Schwarm F.-W., Grinberg V., Obst M., 2013, *A&A*, 551, A6
- Nakajima M., Mihara T., Makishima K., Niko H., 2006, *ApJ*, 646, 1125
- Negueruela I., Okazaki A. T., 2001, *A&A*, 369, 108
- Nishimura O., 2005, *PASJ*, 57, 769
- Orlandini M., Frontera F., Masetti N., Sguera V., Sidoli L., 2012, *ApJ*, 748, 86
- Paul B., Rishin P. V., Maitra C., Gopalakrishna M. R., Duraichelvan R., Ateequlla C. M., Cowsik R., Devasia J., Marykutty J., 2010, in *The First Year of MAXI: Monitoring Variable X-ray Sources* Thomson X-ray Polarimeter for a Small Satellite Mission. p. 68P
- Pottschmidt K., Kreykenbohm I., Wilms J., Coburn W., Rothschild R. E., Kretschmar P., McBride V., Suchy S., Staubert R., 2005, *ApJL*, 634, L97
- Rappaport S., Clark G. W., Cominsky L., Li F., Joss P. C., 1978, *ApJL*, 224, L1
- Romano P., Campana S., Chincarini G., Cummings J., Cusumano G., Holland S. T., et al. 2006, *A&A*, 456, 917
- Santangelo A., Segreto A., Giarrusso S., Dal Fiume D., Orlandini M., Parmar A. N., Oosterbroek T., Bulik T., Mihara T., Campana S., Israel G. L., Stella L., 1999, *ApJL*, 523, L85
- Sartore N., Jourdain E., P. R. J., 2015, *ApJ*, 806, 193
- Sasaki M., Müller D., Kraus U., Ferrigno C., Santangelo A., 2012, *A&A*, 540, A35
- Schönherr G., Schwarm F.-W., Falkner S., Dauser T., Ferrigno C., Kühnel M., Klochkov D., Kretschmar P., Becker P. A., Wolff M. T., Pottschmidt K., Falanga M., Kreykenbohm I., Fürst F., Staubert R., Wilms J., 2014, *A&A*, 564, L8
- Schönherr G., Wilms J., Kretschmar P., Kreykenbohm I., Santangelo A., Rothschild R. E., Coburn W., Staubert R., 2007, *A&A*, 472, 353
- Suchy S., 2011, PhD thesis, University of California, San Diego
- Torréjon J., Schulz N., Nowak M., Kallman T., 2010, *ApJ*, 715, 947
- Tsujimoto M., Guainazzi M., Plucinsky P. P., Beardmore A. P., Ishida M., Natalucci L., Posson-Brown J. L. L., Read A. M., Saxton R. D., Shaposhnikov N. V., 2011, *A&A*, 525, A25
- Tsygankov S. S., Lutovinov A. A., Churazov E. M., Sunyaev R. A., 2007, *Astronomy Letters*, 33, 368
- Verner D. A., Yakovlev D. G., 1995, *A&AS*, 109, 125
- Wilms J., Allen A., McCray R., 2000, *ApJ*, 542, 914